From Signal-based to Impedance-based Sensing: A Paradigm Shift for Plug-and-play, Mobile, and Sensitive Battery-free Sensing

Liyao Li[1], Yun Wu[26], Minsung Kim[3], Bozhao Shang[27], Jie Xiong[4], Wenyao Xu[1], Xiaojiang Chen[25], Yaxiong Xie[1⋄]

[1] University at Buffalo SUNY, [2] Northwest University (China),
[3] Rutgers University, [4] Nanyang Technological University
[5] Shaanxi Key Laboratory of Passive Internet of Things and Neural Computing
[6] Xi'an Key Laboratory of Advanced Computing and Software Security
[7] Shaanxi International Joint Research Centre for the Battery-Free Internet of Things

Abstract

Battery-free sensing has revolutionized IoT applications, but current solutions relying on signal variations between transmitted and backscattered signals remain vulnerable to environmental dynamics and deployment variations. This paper promotes a paradigm shift: inferring targets through antenna impedance variations instead of signal fluctuations, thereby eliminating the impact of unpredictable wireless communication. We demonstrate the effectiveness of this paradigm by reimplementing three existing applications: RIO [1], Keystub [2], and RF-EATS [3]. Compared to original signal-based implementations, our approach shows significant improvements in accuracy and robustness across diverse environments. Furthermore, By integrating antenna engineering with advanced materials science, we also transform antennas into innovative sensors for pressure, temperature, and UV light sensing. This interdisciplinary methodology pushes the boundaries of battery-free sensing, opening new avenues for IoT applications.

CCS Concepts

• **Hardware → Sensor devices and platforms**.

Keywords

Backscatter, RFID, Battery-free, Wireless, Low cost, IOT

⋄ Corresponding author.

ACM MOBICOM '25, Hong Kong, China

ACM ISBN 979-8-4007-1129-9/25/11…$15.00
https://doi.org/10.1145/3680207.3723480

1 Introduction

The emergence of battery-free sensing technology has catalyzed a revolution in the Internet of Things (IoT), significantly expanding our capacity to infuse everyday objects with sensing capabilities. This innovative approach enables a diverse range of applications, from human-object interaction detection [1, 2, 4–6] to environmental monitoring, including temperature sensing [7], gas leakage detection [8], and humidity sensing [9]. Furthermore, battery-free sensing offers a cost-effective method for pervasive object monitoring, facilitating crucial applications such as soil moisture measurement in agriculture [10] and food contamination identification in supply chains [3, 11–13]. By addressing critical challenges in resource-constrained environments, this technology is driving the development of more sustainable and widespread sensing solutions, thereby reshaping the landscape of IoT applications and their real-world impact.

The fundamental principle of battery-free sensing systems lies in the interaction between the backscatter tag and the *sensing target*, such as human presence, temperature changes, or contaminated food. This interaction alters the tag's impedance, which in turn affects how the tag modulates the reflected signal, as illustrated in Figure 1. By interrogating the tag and receiving the backscattered signal, the reader can measure the backscatter channel H_b. Battery-free sensing applications leverage this process by establishing a mapping between the sensing target and the backscatter channel H_b. This mapping enables the inference of the sensing target from the measured backscatter channel [1–4].

The backscatter channel H_b, however, is highly vulnerable to environmental dynamics. As illustrated in Figure 1, H_b comprises three critical components: the forward channel h_{fw} from the reader to the tag, the backward channel h_{bw} from the tag to the reader, and the tag's modulation characteristic h_{tag}, which describes how the tag hardware modulates the reflected signal. This complex composition makes H_b susceptible to various external factors, other than the sensing

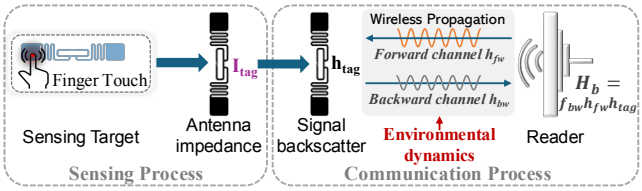

Fig. 1 – Comparison of sensing paradigms. Traditional signal-based sensing relies on a complex sensing-communication chain to correlate the sensing target with the backscatter channel H_b. The impedance-based method directly measures the effect of the sensing target on antenna impedance.

target. Consequently, any alterations in the wireless propagation path, even something as subtle as the rotation of the backscatter tag itself, can significantly affect H_b, potentially leading to misinterpretation by the sensing system.

Such vulnerability introduces a critical challenge: it renders the performance of these sensing systems highly dependent on both the ambient environment and the specific tag-reader deployment configuration, as we have demonstrated through extensive experiments in Section §2.1. This dependence severely compromises the system's reliability and adaptability, making true plug-and-play functionality virtually unattainable in diverse real-world settings.

Extensive efforts have been made to achieve environment- and deployment-independent battery-free sensing systems. Three representative types of solutions have emerged:

- *Reference tag-based solutions* [7, 10, 14, 15] involve placing a reference tag in proximity to the sensing tag. These two tags share the same backward h_{bw} and forward h_{fw} channels but demonstrate different tag-specific impacts h_{tag} on the signal. Consequently, we can leverage the reference tag to eliminate the impact of h_{fw} and h_{bw}, isolating the effect of the interaction between the sensing target and the tag hardware h_{tag}. This approach theoretically achieves environment and deployment independence.
- *Divider-based solutions* [2] utilize one antenna and a power divider to simultaneously power two backscatter chips. As both chips use the same antenna, they share identical wireless propagation channels. This approach employs a principle similar to the reference tag solution, eliminating the impact of wireless propagation channel variations.
- *Machine learning-based approachs* [3] attempt to train neural network models that learn environment-independent features. These models theoretically enable the system to function consistently across various environments by abstracting away the environmental variations in the signal.

We conduct a comprehensive measurement study to validate the deployment dependence of all proposed solutions. Our empirical results reveal that none of these approaches achieves true independence from deployment conditions.

The reference tag-based solution effectively eliminates the impact of backward and forward channels. However, in doing so, it unwittingly releases another demon: mutual coupling between nearby antennas. This coupling effect is inherently deployment-dependent and manifests itself in the estimated channel H_b, ultimately rendering the overall sensing system deployment-dependent, as detailed in Section §2.2. While the divider-based solution exorcises the demon of mutual coupling by using a single antenna, it summons a different set of challenges. First, the unique divider design results in an extremely bulky backscatter tag. Second, this bulky tag hardware imposes strict placement requirements: optimal performance is achieved only when the incoming signal from the reader arrives at the tag perpendicularly, as detailed in Section §2.3. The machine learning-based solution, despite its promise to banish deployment dependence through algorithmic magic, remains shackled to its training data. Our empirical results demonstrate that the trained model fails to generalize effectively to unseen environments where no training data was collected, limiting its practical applicability across diverse settings, as detailed in Section §2.3 and §4.3.

The critical insight of this work is that, as shown in Figure 1, the complex *sensing-communication chain* linking the sensing target to the backscatter channel H_b constitutes the fundamental limitation in current battery-free sensing systems. This chain is susceptible to numerous environmental and deployment factors, which can significantly distort the mapping between the target and the channel, thereby compromising system reliability and adaptability.

To address this foundational challenge, we promote a **paradigm shift** in battery-free sensing, which we term **OhmScanner**. Rather than relying on measurements of the backscatter channel H_b, OhmScanner advocates for directly measuring the impedance variation of the tag antenna (I_{tag}) to infer the sensing target. This approach focuses on the core sensing mechanism: the direct effect of the proximal sensing target on the tag antenna's impedance. By concentrating on this direct interaction between the sensing target and the tag antenna, OhmScanner successfully decouples the sensing and communication processes, circumventing the complexities and vulnerabilities inherent in the traditional sensing-communication chain. This decoupling enables truly plug-and-play battery-free sensing, significantly enhancing the system's adaptability and reliability across environments.

The key enabler for impedance-based OhmScanner is the capability to directly measure the antenna impedance on a battery-free tag. To achieve this, we leverage the impedance tuning capability of commercial backscatter chips [16–19]. This approach hinges on two crucial characteristics of these chips: Firstly, the impedance of these chips are programmable

and known, providing a controllable reference point. Secondly, these chips incorporate impedance-matching algorithms that dynamically adjust their internal impedance to match that of the connected antenna [20]. By exploiting these features, we can simply query the tags for their current impedance values, which directly correlate to and thus allow us to infer the impedance of the antenna.

Revisiting Existing Applications. To validate the transformative potential of our impedance-based sensing paradigm, we reimplement three seminal battery-free sensing applications: RIO for finger touch tracking (§4.1), Keystub for button interaction (§4.2), and ML-based RF-EATS for accurate liquid identification (§4.3). Our comprehensive reimplementation and comparative study reveal groundbreaking improvements across all applications. The impedance-based RIO achieves sub-centimeter finger tracking accuracy under various environments. Similarly, our Keystub variant maintains near-perfect button recognition rates across extreme deployment variations, where the original design fails entirely. Perhaps most strikingly, the reimagined RF-EATS demonstrates over 80% liquid identification accuracy in completely new environments, compared to less than 30% for the original ML model. Crucially, these dramatic enhancements persist across diverse environments, deployment configurations, and even under mobility—scenarios that render traditional approaches unreliable or non-functional. This leap in performance and reliability showcases the paradigm's potential to revolutionize battery-free sensing.

Expanding the Frontiers: Transforming Antennas into Battery-Free Sensors. The proposed impedance-based sensing paradigm offers a new opportunity to transform antennas into versatile, high-sensitivity sensors. By carefully designing antennas or integrating them with materials sensitive to various signals, this approach could significantly expand the frontiers of battery-free sensing. As the initial experimental validation, we enable applications requiring sensitivity levels beyond the capabilities of traditional signal-based solutions through careful antenna designs. Notably, we achieve a breakthrough in liquid sensing: to the best of our knowledge, we are the first to accurately detect liquid concentration using purely an RFID backscatter tag (§5.1).

Furthermore, by leveraging the unique electrical properties of various materials, we unlock a range of novel applications through innovative antenna integrations. We have successfully transformed backscatter tag antennas into diverse sensors: an ultraviolet light sensor by connecting a dipole antenna with a transmission line using a strip made of PIBS-0.75 [21] (§5.2); a pressure sensor by integrating porous nanocomposite (PNC) consisting of CNTs, nanofoam, and PDMS with the antenna (§5.3); and a temperature sensor by incorporating titanium barium ($BaTiO_3$) into the antenna design (§5.3). This interdisciplinary design methodology, combining antenna engineering with advanced materials science, opens new avenues for developing sophisticated battery-free sensing applications, pushing the boundaries of what is possible using battery-free sensing techniques.

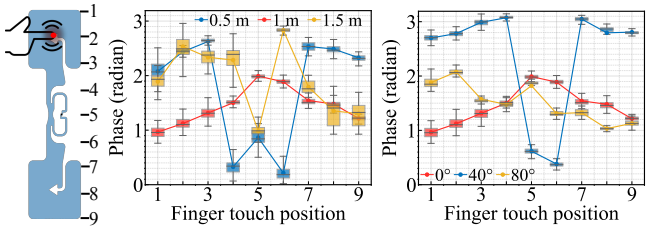

(a) Tag. **(b)** Varying distances. **(c)** Varying tag orientations.

Fig. 2 – The mapping between the measured phase of channel H_b and the finger touch locations under varying tag-reader distances and tag rotations.

2 Traditional Signal-based Sensing

In this section, we introduce the methodology of traditional signal-based battery-free sensing applications and then empirically demonstrate its limitations in providing plug-and-play sensing capability.

2.1 Sensing Methodology and Limitation

2.1.1 Signal Model. In a backscatter system, as illustrated in Figure 1, the communication process involves several key steps. Initially, the reader transmits a signal to the tag, which is reflected back by the RFID tag. Based on the transmitted and backscattered signal, the reader estimates the *backscatter channel* H_b, which consists of three components:

$$H_b = h_{fw} \cdot h_{bw} \cdot h_{tag}. \tag{1}$$

where h_{fw} represents the forward channel from reader to tag, h_{bw} denotes the backward channel from the tag to the reader, and h_{tag} characterizes how the tag hardware modulates the reflected signal.

2.1.2 Sensing Model. The core principle of battery-free sensing is rooted in the interaction between the tag hardware and the *sensing target*. This interaction—be it finger touch, temperature fluctuation, or contact with various materials—modifies the tag-backscattered signal, altering h_{tag} and consequently the overall backscatter channel H_b. In a controlled environment with stable tag hardware, where the forward and backward channels (h_{fw} and h_{bw}) remain constant, the backscatter channel H_b primarily reflects changes in the sensing target. This relationship forms the foundation of our sensing approach: we can quantify the sensing target's attributes through a calibrated mapping between the backscatter channel H_b and the target's specific characteristics. Figure 1 illustrates this concept, presenting an exemplary mapping

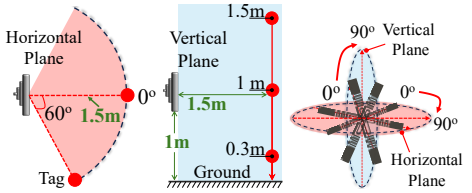

(a) Angle. **(b)** Height. **(c)** Orientation.

Fig. 3 – Tag deployment schematic at different heights, angles, and tag orientations.

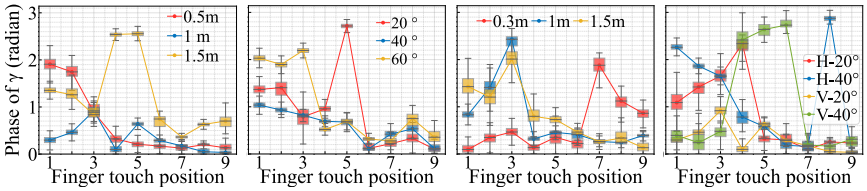

(a) Tag-Reader distance. **(b)** Deploy angle. **(c)** Deploy height. **(d)** Tag orientation.

Fig. 4 – The mapping between γ and the finger touch locations on the antenna with varying tag-reader distance, deployment angle and height, and orientations.

between the backscatter channel and the positions of human finger touches on an RFID antenna.

2.1.3 Limitations: Deployment-dependence and Mobility Constraints. The current method faces a significant practical limitation: deployment dependence. Specifically, the mapping between the backscatter channel H_b and the sensing targets fluctuates with changes in the tag-reader deployment, such as variations in tag-reader distance and tag orientation.

Experimental Verification. To demonstrate this deployment dependence, we conducted a comprehensive experiment. We use a ThingMagic M6 [22] reader and an Dogbone R6 tag [23] in our experiments. We systematically varied the tag's distance from the reader and fingerprinted the mapping between the locations of human finger touches on the tag antenna, as shown in Figure 2a, and the resulting backscatter channel. To ensure robust data capture, we measured the channel 300 times at each location. Additionally, we repeated the experiments with a fixed tag-reader distance (1.5 meter) while altering the tag's orientation in the horizontal plane. All the experiments are conducted in an empty hall (5m × 7m), with no obstacles blocking the LOS (Line of Sight) between the tag and the reader antenna. Such a testbed is optimal for battery-free sensing applications.

Figure 2 illustrates these fingerprinted mappings under various deployment conditions. The results reveal two key findings. First, for a specific deployment configuration (*e.g.*, a fixed tag-reader distance), the mapping remains highly stable, with minimal variation in the measured backscatter channel H_b when the finger touches a particular location. Second, the mapping exhibits significant variations as the deployment configuration changes, underscoring the impact of deployment conditions.

Re-fingerprinting Requirements and Mobility Limitations. To address deployment-dependence, the current system necessitates re-fingerprinting the mapping whenever the deployment configuration changes. This requirement introduces substantial overhead in deploying such solutions. Moreover, the current approach is incompatible with mobility scenarios. In situations involving either reader or tag mobility, the deployment configuration changes continuously, leaving no time for re-fingerprinting. This limitation severely restricts the system's applicability in dynamic environments.

2.2 Attempt to Achieve Deployment Independence with Reference Tag

Recognizing the limitations of existing solutions, particularly their deployment dependence, researchers have explored various approaches to enhance the robustness and flexibility of backscatter sensing systems. One prominent strategy that has emerged from prior works is the use of a reference tag to achieve deployment independence.

2.2.1 Sensing Model. The central concept of this approach involves deploying two tags in close proximity: a *sensing tag* that interacts with the sensing target, and a nearby *reference tag*. The methodology begins by measuring the backscatter channels of both tags: H_b^s for the sensing tag and H_b^r for the reference tag. Next, the ratio of these two measured channels is calculated:

$$\gamma = \frac{H_b^s}{H_b^r} = \frac{h_{fw}^s \cdot h_{bw}^s \cdot h_{tag}^s}{h_{fw}^r \cdot h_{bw}^r \cdot h_{tag}^r}. \tag{2}$$

A crucial assumption is then applied: given the close proximity of the two tags, they share identical forward and backward channels:

$$h_{fw}^s = h_{fw}^r \quad \text{and} \quad h_{bw}^s = h_{bw}^r \tag{3}$$

This assumption simplifies Eqn. 2 to:

$$\gamma = \frac{H_b^s}{H_b^r} = \frac{h_{tag}^s}{h_{tag}^r}. \tag{4}$$

Theoretically, this calculated channel ratio γ becomes independent of the wireless propagation channel, thus achieving deployment independence. The ratio γ solely reflects the difference in tag hardware modulation, with h_{tag}^s influenced by the sensing target. To enable sensing, a new mapping between γ and the sensing target is fingerprinted, allowing the system to interpret γ changes as variations in the sensing target's attributes, *e.g.*, the location of the finger touch.

2.2.2 Experimental Validation. To evaluate the effectiveness of reference tags in achieving deployment independence, we conduct a series of experiments.

Reader-Tag Deployment. We fix the distance between two tags to 2.5 cm and test various reader-tag deployments by varying the following parameters:

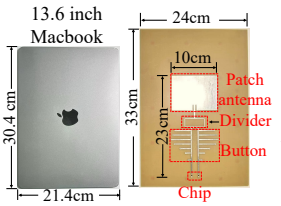

Fig. 5 – The architecture of the Keystub tag.

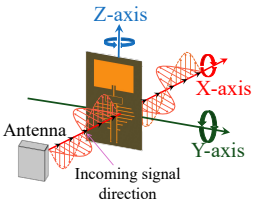

Fig. 6 – The optimal tag-reader deployment.

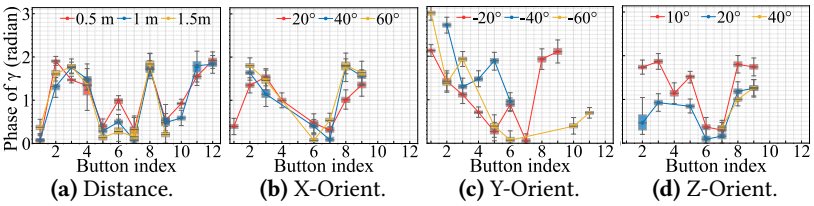

Fig. 7 – The mapping between γ and pressured buttons under varying tag-reader distance and varying tag rotation angles along three axes.

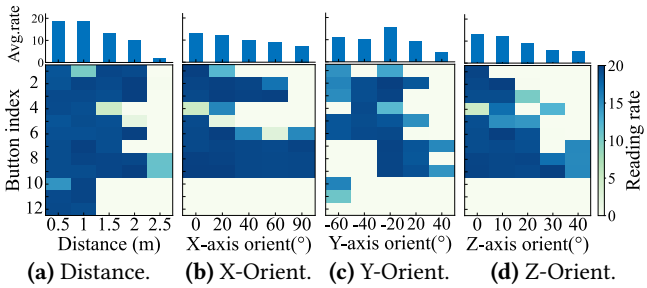

Fig. 8 – The reading rates of each button (*lower*) and the average reading rates of all 12 buttons (*upper*) under varying tag-reader distances and tag rotations along three axes.

- *Reader-tag distance.* We vary the distance between the tag and the reader from 0.5 m to 1.5 m, with a stepsize of 0.5 m.
- *Tag deployment angle.* We fix the reader-tag distance to 1.5 m, but vary the deployment angle of the tag in the horizontal plane. We define the deployment angle where reader's antenna beam is perpendicular to the tag as 0°, as illustrated in Figure 3a,
- *Tag deployment height.* We place the reader at height of 1 m and fix the reader-tag distance to 1.5 m and vary the height of the tag from 0.6 m to 1.5 m, as shown in Figure 3b.
- *Tag orientation.* We place the single tag at a distance of 1 m from the reader, without changing the distance between the tag and the reader antenna. We change the tag orientation by rotating the tag horizontally and vertically just as shown in Figure 3c.

Validation Methodology. To assess deployment independence, we construct a mapping between γ and the sensing target for various deployment configurations. We calculate γ by measuring the backscatter channel in each setup. True deployment independence would be indicated by a consistent mapping across different deployment configurations, including tag-reader distance, deployment height, angle, and tag orientation. Similarly, as our exemplar application, we sense the human finger touch locations on the tag antenna.

Empirical results. Figure 4 illustrates the constructed mapping between the phase of γ and the locations of human finger touches across various deployment configurations Our observations reveal that this mapping still varies across deployments, necessitating recalibration for new configurations. While the reference tag eliminates the impact of forward and backward channels, it introduces another challenge: mutual coupling between antennas in close proximity. This mutual coupling effect changes with tag-reader deployment [24], such as distance and tag orientation, resulting in persistent deployment-dependent sensing performance.

2.3 Eliminating Mutual Coupling with One Antenna and A Power Divider

A recent innovation, Keystub [2], attempts to address the challenge of mutual coupling between the antennas of the sensing tag and reference tag with a single antenna design. Specifically, this approach utilizes a power divider to enable one antenna to energize two RFID chips simultaneously.

Bulky Tag. We fabricated the Keystub tag strictly following the configuration detailed in [2]. Its architecture, shown in Figure 5, consists of one large patch antenna, one power divider to split the received signal, 12 buttons, and two backscatter chips. The overall tag size exceeds that of a 13.6-inch laptop. Although the antenna, the power divider, buttons, and chips occupy only a small portion of the board, the remaining PCB area is crucial for impedance matching. We also fabricated several tags with reduced PCB board sizes, but these were unreadable to the reader even at close range.

2.3.1 Experimental Validation. We experimentally verify the deployment independence of Keystub. We measure the mapping between the channel ratio γ of two chips and the press of 12 buttons, under varying tag-reader distances and tag rotations along three axes, as plotted in Figure 6.

Optimal Deployment. We observe that Keystub performs optimally when configured as shown in Figure 6, ensuring the incoming signal from the reader antenna arrives at the tag perpendicularly. When maintaining this perpendicularity, the mapping remains consistent if we: (**1**) vary the tag-reader distance, as shown in Figure 7a, or (**2**) rotate the tag along the X-axis, as illustrated in Figure 7b. However, rotating the tag along the Y-axis or Z-axis disrupts this perpendicularity, causing variations in the mapping, as evident in Figures 7c and 7. Consequently, the above experimental results demonstrate that Keystub fails to achieve true deployment independence.

Button Reading Rates. Figure 7 also reveals that under various distances and tag rotations, not all 12 buttons are consistently readable. To quantify this, we plot the reading

rate of each button in Figure 8, with a maximum reading rate of 20 Hz. We observe that as the distance increases or the tag orientation deviates further from the perpendicular position (*i.e.*, zero degrees), the button reading rates decrease, with some buttons' rates approaching zero. These experimental results indicate that the Keystub tag and reader need to be carefully placed in order to function correctly.

2.4 Machine Learning based Approach

RF-EATS [3] is a battery-free liquid identification system that explores an alternative approach to achieving deployment independence. The key innovation of RF-EATS lies in training the neural network to learn environment-independent features, theoretically enabling accurate liquid identification across different deployment configurations. Our implementation and experimental results in Section 4.3 demonstrate that RF-EATS's performance remains heavily dependent on the training data and fails to generalize effectively to environments where no training data has been collected.

3 New Paradigm: Impedance-based Sensing

This section introduces a fundamental paradigm shift in battery-free sensing: the transition to impedance-based measurements. We detail our proposed approach, which promises to overcome the limitations of traditional signal-based methods and unlock new sensing possibilities.

3.1 Sensing Methodology

3.1.1 Key Insight. Traditional signal-based sensing, relying on the complex chain linking the sensing target to the backscatter channel H_b (Figure 1), is highly vulnerable to environmental and deployment variations. Our key insight is that the proximal sensing target directly modulates the tag antenna's impedance I_{tag}, which alters the tag's backscattering characteristics h_{tag}. We propose a paradigm shift: directly measuring antenna impedance variations to infer the sensing target, bypassing the unreliable wireless propagation chain.

3.1.2 Direct Antenna Impedance Measurement. Direct antenna impedance measurement is crucial for implementing impedance-based sensing. For static scenarios where the antenna's impedance remains constant, a one-time offline measurement using a Vector Network Analyzer (VNA) suffices. However, measuring impedance variations in real-time with a battery-free tag presents significant challenges due to the severe computational and power constraints

Opportunity: Self-Tuning RFID Chip. We observe that many types of RFID chips [16–19] are capable of adjusting their impedance. These chips implement an impedance-matching algorithm to ensure that the chip's impedance matches the impedance of the antenna to which it is connected. Consequently, when a sensing target affects the antenna's impedance, we can infer the antenna impedance by examining the adjusted impedance of the RFID chip. In our current design, we use Magnus S3 Chip [16] due to its fine-grain impedance adjustment capability. Specifically, Magnus S3 is able to set its impedance to 512 discrete values. [1]

Impedance Matching. The Magnus chip searches within its 512 impedance values for the one that maximizes the received signal strength (RSS), since maximized RSS indicates the highest receiving efficiency and thus optimal impedance matching. This search process occurs during the *tag setting time*, as defined in the C1G2 standard [25]. The sequence unfolds as follows: the reader first powers the tag before communication can begin. After power-up, the tag utilizes a designated setting time to accumulate sufficient energy for communication, during which the reader is prohibited from issuing any commands. By performing impedance matching during this period, the Magnus S3 chip ensures that the tag's impedance is always optimally matched when the reader issues its first command.

Query the Impedance. The chip stores the results of the impedance matching process in a 9-bit register, representing 512 discrete values that can be translated into absolute impedance measurements. The reader can query the tag to retrieve the exact value of this 9-bit register, thereby inferring the tag's impedance.

3.2 RSS-induced Impedance Jitter

3.2.1 Problem: Impedance Jitter. To verify the effectiveness of impedance measurement using the Magnus S3 Chip [16], we measure the impedance of one S3 chip under varying distances and plot the results in Figure 9a. Surprisingly, the measured impedance varies with tag-reader distance, with the variation decreasing as distance increases, seemingly demonstrating deployment dependence. However, a closer examination reveals that this impedance variation is caused by changes in the tag's received signal strength (RSS). To confirm this, we placed the tag 1.5m away from the reader and varied the reader's transmit power while measuring the impedance. The results in Figure 9b confirm that the variation is indeed caused by RSS, rather than distance itself.

We observe that such RSS-induced impedance jitter is ubiquitous among backscatter tags. To verify this, we repeat the above experiment with seven types of tags. Since we cannot directly measure the impedance of these tags, we instead plot the phase of H_b under varying transmit power

[1] The 512 discrete values offered by the chip effectively serves as a 9-bit ADC, enabling sufficiency for the demonstrated applications as evidenced in §4 and §5. Additionally, a 9-bit ADC is adequate for most practical applications.

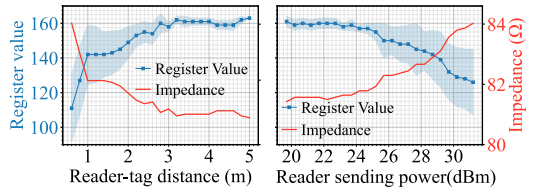

(a) Varying distance. **(b)** Varying send power.

Fig. 9 – The measured tag impedance with varying reader-tag distance and reader sending power.

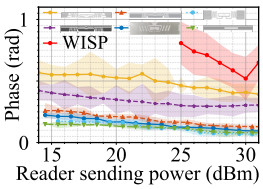

Fig. 10 – Phase varies with different reader sensing power.

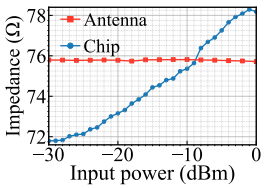

Fig. 11 – Impedance variations stem from chip instead of antenna.

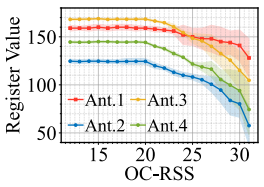

Fig. 12 – The register value variation under different On-Chip RSS.

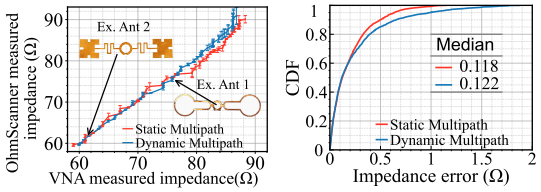

(a) Different scenarios. **(b)** Impedance error.

Fig. 13 – Comparison of OhmScanner and VNA-measured impedance across environments.

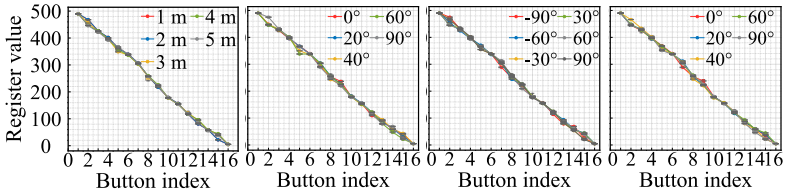

(a) Tag-reader distance. **(b)** X-Orient. **(c)** Y-Orient. **(d)** Z-Orient.

Fig. 14 – The mapping between measured impedance and pressured buttons under varying tag-reader distance and tag rotation angles along three axes.

in Figure 10. Theoretically, the phase of the backscatter channel H_b should remain constant with varying transmit power while keeping all other conditions the same. However, the variations in phase shown in Figure 10 demonstrate corresponding variations in tag impedance across all tested tags.

Impedance Variation Stems from the RFID Chip IC. To identify the source of impedance variation, we separately connected a VNA to a WISP 5 backscatter chip and its antenna. We measured the impedance of both components while varying input power levels from -40 dBm to 0 dBm, with results plotted in Figure 11. We could see from this figure that the antenna impedance remains stable across all power levels, while the chip impedance exhibits changes as power increases. This observation indicates that the impedance variation originates from the chip IC rather than the antenna.

Hypothetical Root Cause: Non-linear RF Components. We propose that the observed impedance jitter can be attributed to the non-linear components inside the backscatter chip, such as diodes, transistors, and other RF components that are widely used in various circuits such as rectifiers, modulators, and power management units. These components exhibit varying impedance under different power levels.

3.2.2 Solution: Dynamic Reader Power Adaptation. To stabilize the impedance readings, we propose to regulate the RSS of the backscatter tag. To achieve this, we need to dynamically adjust the reader's transmit power based on the real-time RSS of the backscatter tag.

Tag Feedback: On-Chip RSS. We observe that the Magnus S3 [16] chip is capable of measuring the tag's RSS, which they term as the *On-Chip RSS* (OC-RSS). This OC-RSS is represented by a 5-bit value, corresponding to 32 discrete RSS levels. Crucially, the reader can query the tag to obtain this real-time OC-RSS information.

Dynamic Power Adaptation. The tag's RSS monotonically increases and decreases with the reader's transmit power, allowing us to control the RSS by simply adjusting the reader's transmit power. The key question is determining the optimal RSS range for control. To find this optimal range, we profiled the relationship between the OC-RSS and the measured tag impedance. To quantify the impact of the antenna, we connected the Magnus S3 chip to four antennas with varying antenna impedances. Figure 12 plots these results, revealing that the measured impedance stabilizes when the OC-RSS falls below 20, and this relationship is analogous across different antenna impedances. To prevent degraded communication performance in a low RSS range while ensuring stable impedance measurements, we empirically set the target OC-RSS range as 17 to 20.

3.3 OhmScanner Experimental Validation

We experimentally validate two key aspects of OhmScanner's direct real-time impedance measurement scheme for battery-free tags: its accuracy and deployment independence.

3.3.1 Accuracy. We conduct an experiment to demonstrate that OhmScanner's direct impedance measurement is capable of accurately measuring tag impedance. We design and fabricate 70 antennas with varying impedances. Our measurement process involves two steps. First, we use a VNA to measure each antenna's impedance by directly connecting it, considering this as the ground truth. Subsequently, we solder each antenna to the chip and use the reader to query the chip for impedance 300 times. This second measurement is performed under two conditions: in a static office environment and with people walking randomly near the tag.

Figure 13 directly compares the impedance measurements for each antenna. We observe that OhmScanner's impedance

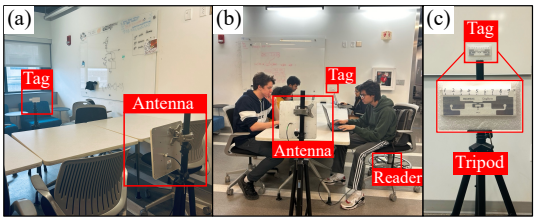

Fig. 15 – Static (**a**) and dynamic office (**b**) environment. The unstable tag mount is shown in (**c**).

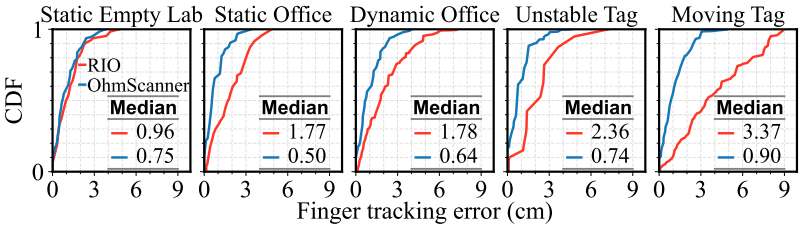

Fig. 16 – The finger tracking accuracy of RIO and OhmScanner in various environments. The maximum error is 10 cm, *i.e.*, antenna length.

measurements closely align with those measured by the VNA, with median errors of 0.118 Ω and 0.122 Ω for the static and mobile tests, respectively. It's important to note that soldering the antenna to the chip introduces additional impedance variations captured by OhmScanner's measurements. Consequently, we believe the actual accuracy of OhmScanner may be even higher than these results suggest.

3.3.2 Deployment-Independence. We have designed a OhmScanner-based Keystub equivalent button board containing 16 buttons, as detailed in Section §4.2. To evaluate the deployment independence of OhmScanner's impedance measurement, we profile the relationship between the measured tag impedance and the press of 16 buttons while varying the tag-reader distance and rotating the tag along three axes, similar to the setup in Figure 6. Figure 14 illustrates the constructed mapping, where the y-axis represents the 9-bit register value corresponding to the antenna impedance, and the x-axis describes the press of 16 buttons. We observe that this mapping remains remarkably consistent across all different deployment configurations, exhibiting only minor variations. This high level of consistency across varying deployments demonstrates the robustness of our approach and paves the way for truly plug-and-play battery-free sensing.

4 Revisiting Existing Applications

This section presents a comparative analysis of three existing signal-based applications reimplemented using our proposed impedance-based battery-free sensing paradigm: RIO for finger touch tracking, Keystub for human interaction with a battery-free button board, and ML-based RF-EATS for liquid identification. Through head-to-head comparisons, we demonstrate the superiority of impedance-based sensing over traditional signal-based approaches. We collectively refer to these reimplemented applications as OhmScanner for consistency and simplicity throughout our analysis.

4.1 Finger Touch Tracking (RIO)

Methodology and Implementation of RIO. RIO [1] transforms RFID tags into interactive, touch-sensitive interfaces by mapping the measured backscatter channel H_b to finger locations on the RFID antenna. Our implementation utilizes an Aline-9640, Higgs-3 tag [26]. For signal transmission and backscatter channel estimation, we employ an Impinj Speedway R420 Reader [27] with a 9 dBi gain antenna [28].

Implementation of OhmScanner Enhanced RIO. The OhmScanner-enhanced RIO implementation retains the original RFID tag antenna but replaces the backscatter chip with Magnus S3 [29]. For impedance querying, we utilize the ThingMagic M6 Mercury reader [22]. Analogous to RIO, we establish a mapping between measured impedance and finger touch locations to enable touch tracking.

Experimental Setup. To thoroughly evaluate finger-tracking performance under various environmental conditions with varying levels of channel dynamics and multipath reflections, we conduct experiments using the following configurations:

- *Static empty lab:* Experiments are conducted in an empty lab space with scarce multipath reflections. The tag and reader remain static during the whole experiment.
- *Static office:* An office room furnished with many desks and chairs, as shown in Figure 15a. expecting rich multipath reflections. Tag and reader are static, with no human movement allowed during the experiment.
- *Dynamic office:* Volunteers walk randomly in the office room, creating dynamic reflections, as shown in Figure 15b.
- *Unstable tag mount:* Tag placed on an unstable panel in the office room, as shown in Figure 15c. Finger touches induce panel vibrations, resulting in subtle tag movements.
- *Moving tag:* The tag moves at a constant speed of 5 cm/s while tracking fingers. Experiments are conducted in the office with volunteers moving around, combining tag mobility with environmental dynamics.

For each scenario, we test 10 different locations. At each location, we first calibrate RIO by recollecting its mapping, followed by 100 times finger swipes. In contrast, we collect the mapping for OhmScanner only once at the beginning of the experiment, without any subsequent recalibration.

Tracking Accuracy. Figure 16 illustrates the tracking accuracy of RIO and OhmScanner. In a static, low-multipath environment, both methods demonstrate comparable accuracy, with median errors of 0.75 cm and 0.96 cm for RIO and OhmScanner, respectively. However, RIO's tracking accuracy deteriorates rapidly with increasing static and dynamic multipath reflections and enhanced mobility. In contrast, OhmScanner maintains robust performance across environments

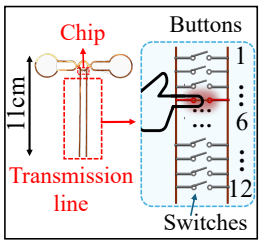

Fig. 17 – OhmScanner tag comprises a chip and two transmission lines.

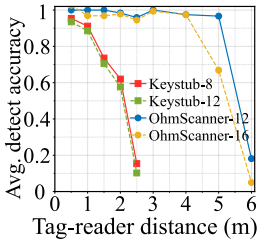

Fig. 18 – The button recognition accuracy at varying distances.

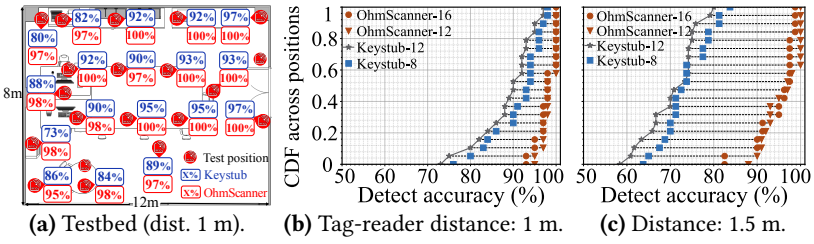

(a) Testbed (dist. 1 m). **(b)** Tag-reader distance: 1 m. **(c)** Distance: 1.5 m.

Fig. 19 – The distribution of button recognition accuracy when the tag is placed at various locations with the tag-reader distance of 1.5m (**a**). The CDF of accuracy when the tag-reader distance is 1 m (**b**)and 1.5 m (**c**).

with varying levels of multipath and mobility, even without recalibration. This level of consistency demonstrates OhmScanner's truly environment- and deployment-independent battery-free sensing capability.

4.2 Keyboard Interface (Keystub)

Implementation of Keystub. We replicated the Keystub [2] battery-free button board as per the original configuration (Figure 5). Our implementation measures the backscatter channel of two tags, calculates γ, and applies the button recognition algorithm as described in [2].

OhmScanner-Based Keystub-Equivalent Button Board. We designed a button board functionally identical to Keystub using a commercial Magnus S3 chip [30] and a custom antenna comprising a dipole and two transmission lines (Figure 17). To match Keystub's 12-button functionality, we incorporated 12 evenly distributed copper strips as switches connecting the two power lines. Button presses connect these lines; otherwise, they remain disconnected. We also developed a 16-button version, extending the same principle with 16 evenly distributed copper strip-based switches.

Experimental setup. We conducted experiments in an office room furnished with desks and chairs (Figure 19a). Performance tests for both Keystub and OhmScanner were carried out at 12 locations within the room. To optimize Keystub's performance, we positioned its tag and reader with zero-degree rotation along all axes, ensuring *perpendicular signal arrival*. For OhmScanner, we tested different tag rotations along three axes at each location. All tests were performed at two tag-reader distances: 1 meter and 1.5 meters.

Button Recognition Accuracy. We calculated the average recognition accuracy of all buttons for each testing location. For Keystub, we analyzed two versions: the original 12-button configuration and a derived 8-button version, which averages only the eight highest-performing buttons [2]. For

[2]Designing a Keystub tag with only eight physical buttons requires a comprehensive redesign of the entire hardware architecture, a complex and resource-intensive process beyond the scope of this study.

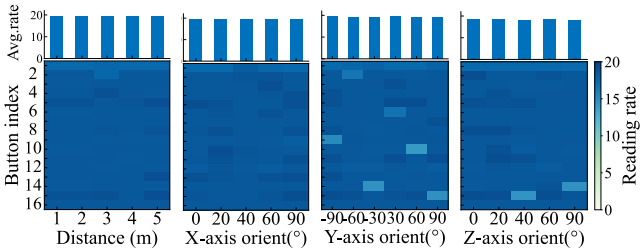

(a) Distance. **(b)** X-Orient. **(c)** Y-Orient. **(d)** Z-Orient.

Fig. 20 – OhmScanner's reading rates of each button (*lower*) and average reading rates of all 16 buttons (*upper*) under varying tag-reader distances and rotations along three axes.

OhmScanner, we tested and calculated results for both the implemented 12-button and 16-button versions.

We plot the button recognition accuracy of two systems under varying tag-reader distances in Figure 18. The results demonstrate that OhmScanner maintains an accuracy higher than 90% when the tag is placed up to 4 m and 5 m away from the reader for the 12-button and 16-button versions, respectively. This performance clearly illustrates the successful decoupling of communication and sensing in our approach. In contrast, Keystub's accuracy steadily decreases with distance, becoming non-functional beyond 2.5 m.

We also plot a head-to-head comparison between the two systems at all 20 locations in Figure 19. Specifically, Figure 19a and b show the results when the tag-reader distance is 1m. These results demonstrate that OhmScanner achieves higher than 90% accuracy at every location, consistently outperforming Keystub. More surprisingly, the 16-button version of OhmScanner outperforms even the 8-button version of Keystub across all locations. Figure 19c illustrates that the performance gap significantly widens when the tag-reader distance increases to 1.5 m. Notably, this superior accuracy is achieved under conditions that inherently favor Keystub: we fixed Keystub's tag-reader orientation without any rotation to ensure perpendicular signal arrival at each location, while for OhmScanner, we rotated the tag along three axes. This unfair comparison further underscores the robustness and versatility of OhmScanner's performance.

(a) Experimental settings in [3]. **(b)** OhmScanner setting.

Fig. 21 – The system implementation and experimental setting of RF-EATS and OhmScanner.

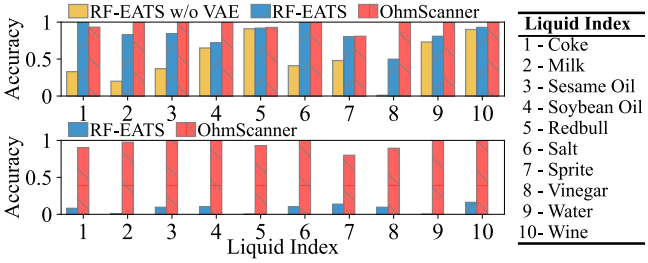

Fig. 22 – Overall performance with different methods. RF-EATS training and testing in the same environment *(upper)*. RF-EATS training in two environments and testing in three different environments *(lower)*.

Button Reading Rate. We also plot OhmScanner's button reading rate in Figure 20. The results demonstrate that OhmScanner maintains a high reading rate across varying tag-reader distances and tag rotations along all three axes.

4.3 Liquid Sensing (RF-EATS)

Methodology of RF-EATS. RF-EATS [3] is a sensing system designed to verify the authenticity of food and liquids without opening their containers. The system operates by attaching an RFID tag to the container and measuring the backscatter channel H_b to identify the liquid inside. RF-EATS incorporates two key design elements: first, a neural network that learns environment-independent features for liquid identification, and second, variational autoencoders (VAEs) that generate realistic synthetic multipath data for model training. Theoretically, these components enable RF-EATS to achieve robust sensing across various environmental conditions. We have replicated the system implementation of RF-EATS as described in [3], using identical hardware, including two USRPs and four antennas, as shown in Figure 21a.

OhmScanner based Liquid Sensing. Our approach similarly attaches an RFID tag to the food container and uses a ThingMagic M6 mercury reader to query tag impedance. We sweep the reader's operating frequency from 902.75 MHz to 927.25 MHz in 0.5 MHz increments, covering 50 channels. Each frequency yields one tag impedance measurement, resulting in a 50-dimensional impedance vector. This vector serves as the feature for liquid identification. We construct a fingerprint database of various liquids and employ dynamic time warping (DTW) to match new measurements against this database for identification. The implementation of OhmScanner based liquid sensing system is shown in Figure 21b. Notably, OhmScanner utilizes a much lighter hardware setup than RF-EATS, requiring only one reader and one antenna.

Testbeds and Liquids. We evaluate the systems across three distinct environments: an office room furnished with twelve chairs and desks, an activity room containing a sofa and various furniture pieces, and a classroom densely populated with desks and chairs. Our tests involve identification 10 types of liquids, as detailed in Figure 22.

Training and Testing in the Same Environment. We use data collected from all three environments to train RF-EATS, with an 80-20 split for training and test data. We train two versions of RF-EATS: one using only data collected from the three testbeds, and another incorporating both collected and VAE-synthesized data. Figure 22 *upper* illustrates the identification accuracy of 10 liquids for both RF-EATS versions and OhmScanner. We observe two key findings: First, the synthesized data indeed enhances the neural network's accuracy for RF-EATS, yielding an average improvement of 33.5%. Second, OhmScanner consistently outperforms the VAE-enhanced RF-EATS for nine out of ten liquids, with the exception of coke. On average, OhmScanner's liquid identification accuracy surpasses that of RF-EATS by 13.2%.

Generalization to Unseen Environments. To test the generalization of the trained model, we retrained RF-EATS using data collected from the office room and activity room, along with VAE-synthesized data, but evaluated its accuracy using data from the classroom. Figure 22 *(lower)* illustrates the identification accuracy of both RF-EATS and OhmScanner. Surprisingly, we observe that RF-EATS's detection accuracy decreases dramatically in the unseen environment, with many liquids approaching zero accuracy[3]. In contrast, OhmScanner maintains consistently high detection accuracy across all environments. On average, OhmScanner outperforms RF-EATS by 87% in this generalization test.

Takeaway. ML-based sensing heavily rely on high-quality training data and struggle to generalize to unseen environments, limiting their ability to support plug-and-play battery-free liquid sensing. In contrast, impedance-based solutions demonstrate immunity to changes in wireless propagation environments, offering a robust and versatile approach.

5 Expanding the Frontiers: Transforming the Antenna into Battery-Free Sensor

This section demonstrates how impedance-based sensing significantly expands the frontiers of battery-free sensing. Leveraging our highly-sensitive impedance measurement scheme, we enable diverse sensing applications by making

[3]The open-source implementation, trained model, and data are available at: https://github.com/NEMO-LAB-repo/Reproduce_RFEats

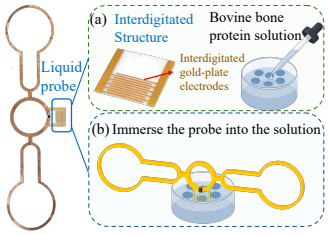

Fig. 23 – Schematic of OhmScanner integrated with a liquid probe for protein sensing.

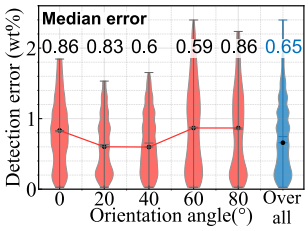

Fig. 24 – Detection error of protein concentration under varying tag orientations.

the antenna impedance responsive to various sensing targets. We showcase two key approaches to achieve this: careful antenna design tailored to specific sensing requirements, and integration of antennas with materials sensitive to various signals. These complementary strategies harness the full potential of impedance-based sensing, opening up new possibilities for battery-free applications across domains.

5.1 Liquid Concentration Sensing

Detection Mechanism. Different types of liquids, as well as different concentrations, exhibit varying permittivity [3, 11–13]. We integrate an interdigitated structure as a liquid probe on the OhmScanner antenna as shown in Figure 23. This structure consists of closely spaced, interdigitated gold-plate electrodes, forming a capacitor, as shown in Figure 23a. When the liquid contacts the probe, the capacitance of the probe changes according to the liquid's permittivity, which in turn alters the antenna impedance. We use bovine bone protein solutions as an example and immerse the liquid probe into varying concentrations solutions, as shown in Figure 23b.

Performance Evaluation. We set the distance between the reader and the OhmScanner to 1 m and test the performance of the OhmScanner with protein concentrations ranging from 1 wt% to 15 wt%. To further evaluate the OhmScanner's performance, particularly its independence from environmental factors, we rotate the tag at different orientations, from 0° to 80° in 20° increments. As shown in Figure 24, the detection error ranges from 0.6 wt% to 0.86 wt%, with an overall performance of 0.65 wt%.

5.2 Antenna as a UV Light Sensor

UV Exposure Duration time Sensing Mechanism. The PIBS-0.75 [21] is a unique material for sensing UV irradiation duration, as shown in Figure 25. When exposed to UV light, the azobenzene units within the material, depicted in Figure 25b, undergo photo trans-cis isomerization [31], leading to a change in the molecular structure that causes bending deformation of the material. This deformation is dependent on both the duration and intensity of UV exposure. PIBS-0.75 ability to respond to UV light and stop responding immediately once the exposure ceases, effectively sensing and recording the duration of UV exposure.

OhmScanner Implementation for UV exposure duration sensing. We leverage the material's unique response to UV light by integrating PIBS-0.75 with the OhmScanner, as shown in Figure 25a, to create a battery-free UV light detection tag. The OhmScanner tag is designed to consist of a dipole antenna, a coupling line, and PIBS-0.75. We position PIBS-0.75 between the dipole antenna and the coupling line. In its initial state, the dipole antenna is parallel to the coupling line. After UV exposure, the structure of PIBS-0.75 changes based on the exposure time, altering the angle between the dipole antenna and the coupling line. As shown in Figure 25c, when the angle between the dipole antenna and the coupling line changes, the radiation pattern and surface current are altered accordingly, which in turn leads to a change in the overall antenna impedance.

Performance Evaluation. We use a 365nm UV light with constant power as the UV light source. The tag is hung on a shelf and exposed to the UV light. When the UV light is turned on, a clock starts to record the exposure time as the ground truth. The reader antenna is positioned 1 m away to simultaneously record the measured impedance. We test the exposure time for 1 minutes, then turn off the UV light and heat the material to 60° until it returns to its initial shape before starting the next round. This process is repeated 50 times. The result is shown in Figure 26a and 26b. The OhmScanner measures UV light exposure time with an error ranging from 1.31 s to 2.3 s at varying distances from 0.5 m to 2.5 m, and with an error ranging from 1.3 s to 1.74 s at different orientation angles. The overall performance shows a UV exposure time error of 1.76 s and 1.56 s across different distances and orientation angles, demonstrating OhmScanner's robustness and independence from environmental conditions.

5.3 Antenna as a Pressure Sensor

Pressure Sensing Mechanism. Carbon nanotubes (CNTs) is a piezoresistive material that exhibits a microscale tubular structure. The resistance of the CNTs decreases as the applied pressure increases. The pressure sensor embedded in the tag is a highly porous nanocomposite (PNC) consisting of CNTs, nanofoam, and PDMS just as shown in Figure 27c. The working mechanism of this pressure sensor is not only related to the piezoresistive response of CNTs but also involves a capacitive change principle. Specifically, when pressure is applied to the sensor, the porosity of the PNC structure changes, leading to a change in the permittivity of the medium, which ultimately results in a change in the overall capacitance.

OhmScanner Implementation for Pressure Sensing. We use a patch with a diameter of 6mm to clamp the CNT@PDMS,

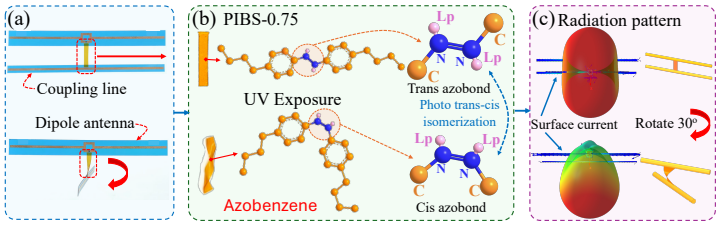

Fig. 25 – The schematic of OhmScanner integrated with PIBS-0.75 material performance for UV exposure duration sensing.

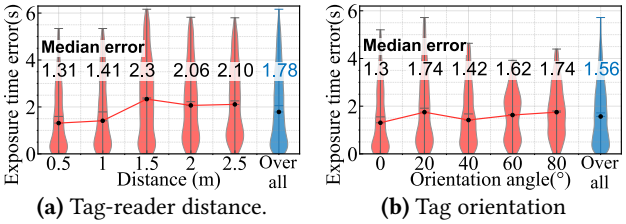

(a) Tag-reader distance. **(b)** Tag orientation

Fig. 26 – The exposure time error of OhmScanner in different detect distances and different orientation angles.

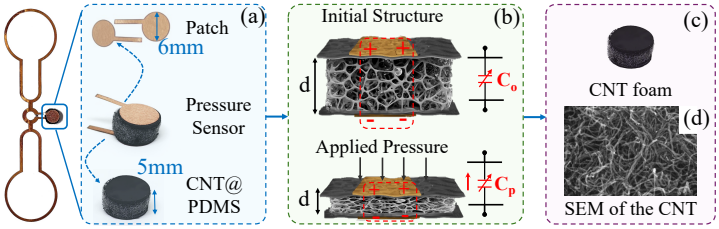

Fig. 27 – The schematic of OhmScanner integrated with CNT@PDMS material as a pressure sensor for pressure sensing.

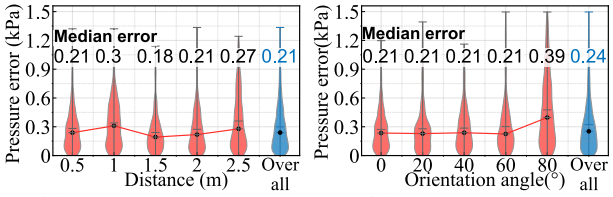

(a) Tag-reader distance. **(b)** Tag orientation.

Fig. 28 – The pressure error under different reader-to-tag distance and orientation angles.

forming a capacitor just as shown in Figure 27a. The size of the pressure sensor is a cylindrical structure with a 6mm radius and a 5mm thickness. When external pressure is applied to the tag, the distance between the patches decreases, causing a change in the capacitance of the pressure sensor. Once the pressure is reduced, the foam structure helps the sensor recover to its initial state.

Performance Evaluation. We leverage a commercial pressure sensor to measure the ground truth and compare it with the pressure measured by OhmScanner. The overall measurement range is 0 - 12 kPa. We evaluate the performance of OhmScanner across various reader-to-tag distances and orientations, with the results shown in Figure 28a and 28b. The overall performance of pressure sensing at different distances and orientations is 0.21 kPa (within a range of [0.18,0.3] kPa) and 0.24 kPa (within a range of [0.21,0.39] kPa), which is sufficient for biomedical sensing applications [32–35].

5.4 Antenna as a Temperature Sensor

Temperature Sensing Mechanism. The titanium barium ($BaTiO_3$) [36, 37] is a ceramic material with a tetragonal crystal structure, as shown in Figure 29b and 29c. As the temperature increases, the tetragonal crystal structure transitions from the form shown in Figure 29b(*upper*) to 29b(*bottom*). The structure change alters the material's permittivity, which in turn affects the capacitance of the temperature sensor.

OhmScanner Implementation for Temperature Sensing. OhmScanner sensor is fabricated with the following steps: Firstly, 1.5 g $BaTiO_3$ powder is dispersed into the 10 g PDMS solution, with a ratio of 1:10 for the PDMS curing agent to the solution. The mixture is then poured into a 1 mm thick template and heated at 70 °C for 30 minutes to form the $BaTiO_3$ film. Finally, two copper patches clamp the $BaTiO_3$ film to create the temperature sensor, just as shown in Figure 29a.

Performance Evaluation. We employ a digital hotplate to precisely regulate the temperature from 25 °C to 95 °C. Concurrently, the temperature is measured by the OhmScanner and we compare the readings to calculate the temperature error. The results obtained from this experimental setup are illustrated in Figure 30a and 30b. With varying detection distance and tag orientation angles, OhmScanner shows stable performance within a temperature median detection error range of [1.47,1.8] °C across different distances and [1.57,1.82] °C across different orientation angles.

6 Related work

Backscatter Tag as the Sensor. Previous research has explored various battery-free sensing applications, one of which involves utilizing the backscatter tag as the sensor. This includes human-object interaction[1, 4, 38–44], where tags are used as UI surfaces or keyboards, with backscatter channel changes tracking touch position. Environmental monitoring applications [8, 45], such as temperature[7], humidity [9], soil moisture sensing [10], chemical [45] and gas sensing[8, 46], involve self-designed tags for sensing purposes. Food sensing [3, 11–13, 47, 48], liquid height or leakage detection [15, 49, 50] similarly uses tags to detect changes in materials by altering the tag's impedance. All of the works use the tag as the sensor, detecting changes in the backscatter channel to indicate changes in the sensing target which is highly vulnerable to environmental dynamics. Recent methods like differential minimum response threshold (DMRT) and minimum response threshold (MRT) [10, 51] utilize minimum reader transmission power to active tags, but remain

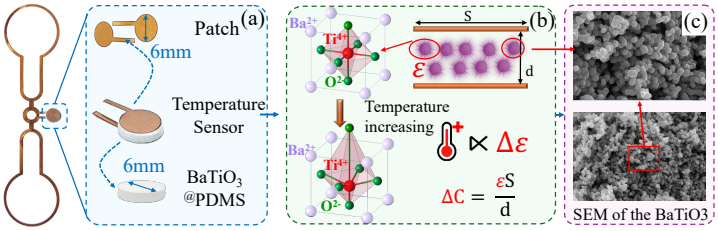

Fig. 29 – The schematic of OhmScanner integrated with $BaTiO_3$@PDMS as a sensor for temperature sensing.

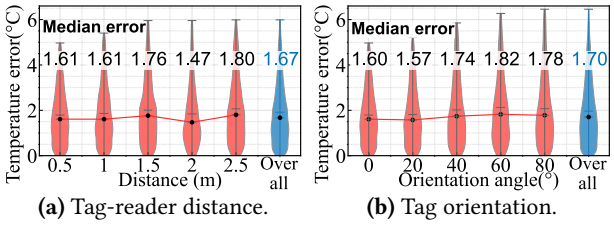

(a) Tag-reader distance. **(b)** Tag orientation.

Fig. 30 – The temperature error under different reader-to-tag distances and orientation angles.

fundamentally reliant on backscatter signals with significant limitations. The limitations include poor real-time performance, as DMRT and MRT require 0.1 - 7.2 s for each estimation, making them unsuitable for applications like gesture tracking where need immediate response; restricted detection range, with most studies reporting a maximum range of 2 m; and low resolution for environmental variables, such as a temperature resolution of 20^oC. OhmScanner focuses on directly measuring impedance variations of the sensing target, ensuring it is environment and deployment-independent.

Sensing the Backscatter Tag. Aside from applications where the backscatter tag serves as the sensor, there is a significant amount of work focused on sensing the backscatter tag to perform tasks such as high-speed rotation monitoring [52, 53], and RF based tracking [54–56] especially tracking the position [55, 57–62] or object rotation angle [63, 64]. In all of these cases, the tag does not change, with variations in the backscatter channel being detected. This approach falls outside the scope of comparison for our method.

Direct Impedance measurement method. Several works share a similar approach by directly measuring impedance for various applications. Cyclops [17] measures eye pressure by directly measuring impedance. Work [65] utilizes self-tunable RFID chips to detect variations in the dielectric permittivity of a substrate, with potential applications in monitoring food freshness. Work [66] employs temperature-sensitive materials, leveraging a self-tuning RFID chip for temperature sensing. Work [67] designs an epidermal antenna and integrates a self-tuning chip for skin temperature sensing. All of these works primarily contribute to application-specific innovations. NFCapsule [68] adopts an RLC resonant circuit combined with near-field coupling technology to measure changes in biological tissue impedance.

OhmScanner provides a more systematic comparison and rigorous evaluation, making significant experimental contributions and conducting a detailed comparative analysis. It expands the design space of existing impedance-based sensing systems. Through comprehensive experiments, OhmScanner decouples the sensing process from the communication chain and demonstrates robust performance under diverse environmental and deployment conditions.

7 Practical Deployment Discussion

OhmScanner deploys a commercial RFID reader and commercial RFID chip [16] to demonstrate the effectiveness of impedance-based sensing. Both the reader and the chip comply with the EPC standard [25]. The custom tag antenna design follows standard antenna engineering principles, with a primary focus on optimizing impedance matching between the antenna and the chip. While various sensing modalities (e.g., pressure sensing, temperature sensing) necessitate impedance re-optimization between the chip and tag antenna, such adjustments are implemented through well-established and mature antenna design methodologies that fall beyond the scope of this study. Therefore, OhmScanner remains highly adaptable and scalable for various sensing applications without introducing extra design complexity.

8 Conclusion

This work promotes a paradigm shift in battery-free sensing by directly measuring antenna impedance variations. Our approach decouples sensing from communication, addressing fundamental limitations of traditional methods. We demonstrate significant improvements in accuracy and robustness across diverse applications, while enabling novel sensing capabilities through advanced materials integration. This interdisciplinary approach not only enhances existing applications but opens new avenues for battery-free IoT sensing.

Acknowledgments

This work is supported by the National Natural Science Foundation of China (62272388) and the Shaanxi Science and Technology Innovation Team Program under Grant (2024RSCXTD05). This work is also supported by Yaxiong Xie's startup funding. We thank our shepherd and anonymous reviewers for their insightful feedback which helped improve this paper.

References

[1] Swadhin Pradhan, Eugene Chai, Karthikeyan Sundaresan, Lili Qiu, Mohammad A Khojastepour, and Sampath Rangarajan. Rio: A pervasive rfid-based touch gesture interface. In *Proceedings of the 23rd Annual International Conference on Mobile Computing and Networking*, pages 261–274, 2017.

[2] John Nolan, Kun Qian, and Xinyu Zhang. Keystub: A passive rfid-based keypad interface using resonant stubs. *Proceedings of the ACM on Interactive, Mobile, Wearable and Ubiquitous Technologies*, 7(4):1–23, 2024.

[3] Unsoo Ha, Junshan Leng, Alaa Khaddaj, and Fadel Adib. Food and liquid sensing in practical environments using rfids. In *17th USENIX Symposium on Networked Systems Design and Implementation (NSDI 20)*, pages 1083–1100, 2020.

[4] Chuhan Gao, Yilong Li, and Xinyu Zhang. LiveTag: Sensing Human-Object interaction through passive chipless WiFi tags. In *15th USENIX Symposium on Networked Systems Design and Implementation (NSDI 18)*, pages 533–546, Renton, WA, April 2018. USENIX Association.

[5] Agrim Gupta, Cédric Girerd, Manideep Dunna, Qiming Zhang, Raghav Subbaraman, Tania Morimoto, and Dinesh Bharadia. WiForce: Wireless sensing and localization of contact forces on a space continuum. In *18th USENIX Symposium on Networked Systems Design and Implementation (NSDI 21)*, pages 827–844, 2021.

[6] Bryce Kellogg, Vamsi Talla, and Shyamnath Gollakota. Bringing gesture recognition to all devices. In *Proceedings of the 11th USENIX Conference on Networked Systems Design and Implementation*. USENIX Association, 2014.

[7] Swadhin Pradhan and Lili Qiu. Rtsense: Passive rfid based temperature sensing. In *Proceedings of the 18th Conference on Embedded Networked Sensor Systems*, pages 42–55, 2020.

[8] Xue Sun, Jie Xiong, Chao Feng, Xiaohui Li, Jiayi Zhang, Binghao Li, Dingyi Fang, and Xiaojiang Chen. Gastag: A gas sensing paradigm using graphene-based tags. In *Proceedings of the 30th Annual International Conference on Mobile Computing and Networking*, pages 342–356, 2024.

[9] Sabina Manzari, Cecilia Occhiuzzi, Shankar Nawale, Alexandro Catini, Corrado Di Natale, and Gaetano Marrocco. Humidity sensing by polymer-loaded uhf rfid antennas. *IEEE Sensors Journal*, 12(9):2851–2858, 2012.

[10] Ju Wang, Liqiong Chang, Shourya Aggarwal, Omid Abari, and Srinivasan Keshav. Soil moisture sensing with commodity rfid systems. In *Proceedings of the 18th International Conference on Mobile Systems, Applications, and Services*, pages 273–285, 2020.

[11] Unsoo Ha, Yunfei Ma, Zexuan Zhong, Tzu-Ming Hsu, and Fadel Adib. Learning food quality and safety from wireless stickers. In *Proceedings of the 17th ACM workshop on hot topics in networks*, pages 106–112, 2018.

[12] Ju Wang, Jie Xiong, Xiaojiang Chen, Hongbo Jiang, Rajesh Krishna Balan, and Dingyi Fang. Tagscan: Simultaneous target imaging and material identification with commodity rfid devices. In *Proceedings of the 23rd Annual International Conference on Mobile Computing and Networking*, pages 288–300, 2017.

[13] Binbin Xie, Jie Xiong, Xiaojiang Chen, Eugene Chai, Liyao Li, Zhanyong Tang, and Dingyi Fang. Tagtag: material sensing with commodity rfid. In *Proceedings of the 17th conference on embedded networked sensor systems*, pages 338–350, 2019.

[14] Ju Wang, Liqiong Chang, Omid Abari, and Srinivasan Keshav. Are rfid sensing systems ready for the real world? In *Proceedings of the 17th Annual International Conference on Mobile Systems, Applications, and Services*, pages 366–377, 2019.

[15] Junchen Guo, Ting Wang, Yuan He, Meng Jin, Chengkun Jiang, and Yunhao Liu. Twinleak: Rfid-based liquid leakage detection in industrial environments. In *IEEE INFOCOM 2019-IEEE Conference on Computer Communications*, pages 883–891. IEEE, 2019.

[16] Magnus-3. https://www.axzon.com/packagedQFN.html.

[17] Liyao Li, Bozhao Shang, Yun Wu, Jie Xiong, Xiaojiang Chen, and Yaxiong Xie. Cyclops: A nanomaterial-based,battery-free intraocular pressure (iop) monitoring system inside contact lens. In *21st USENIX Symposium on Networked Systems Design and Implementation (NSDI 24)*, pages 1659–1675, 2024.

[18] Impinj monza r6 series rain rfid tag chips. https://www.impinj.com/products/tag-chips/impinj-monza-r6-series.

[19] Ucode 8/8m. https://www.nxp.com/products/rfid-nfc/ucode-rain-rfid-uhf/ucode-8-8m:SL3S1205-15.

[20] Shahriar Rokhsaz. Method and apparatus for varying an impedance, December 20 2011. US Patent 8,081,043.

[21] Zhishuai Cui, Xiaolei Yue, Yucheng Wang, Yujie Zhang, Zhi-Hui Ren, and Zheng-Hui Guan. A light-responsive poly (urethane-urea) actuator with room temperature self-healing performance. *Chemical Engineering Journal*, 479:147538, 2024.

[22] Thingmagic mercury 6 4-port enterprise uhf rfid reader. https://www.barcodesinc.com/media/pdf/ThingMagic/m6.pdf.

[23] Ad dogbone. https://rfid.averydennison.com/en/home/product-finder/dogbone.html.

[24] Hema Singh, HL Sneha, and RM Jha. Mutual coupling in phased arrays: A review. *International Journal of Antennas and Propagation*, 2013(1):348123, 2013.

[25] Epc radio-frequency identity protocols generation-2 uhf rfid. https://www.gs1.org/sites/default/files/docs/epc/uhfc1g2_1_2_0-standard-20080511.pdf.

[26] Alien squiggle inlay. https://www.alientechnology.com/products/tags/squiggle/.

[27] Impinj speedway rain rfid readers for flexible solution development. https://www.impinj.com/products/readers/impinj-speedway.

[28] Vulcan rfid™ race timing antenna kit. https://www.atlasrfidstore.com/vulcan-rfid-race-timing-antenna-kit-15-ft-cable/.

[29] Ad temperature sensor dogbone. https://rfid.averydennison.com/en/home/product-finder/temperature-sensor-dogbone.html.

[30] Magnus s3. https://www.axzon.com/packagedQFN.html.

[31] Xinlei Pang, Jiu-an Lv, Chongyu Zhu, Lang Qin, and Yanlei Yu. Photodeformable azobenzene-containing liquid crystal polymers and soft actuators. *Advanced Materials*, 31(52):1904224, 2019.

[32] Lekshmi A Kurup, Cameron M Cole, Joshua N Arthur, and Soniya D Yambem. Graphene porous foams for capacitive pressure sensing. *ACS Applied Nano Materials*, 5(2):2973–2983, 2022.

[33] Mickaël Pruvost, Wilbert J Smit, Cécile Monteux, Philippe Poulin, and Annie Colin. Polymeric foams for flexible and highly sensitive low-pressure capacitive sensors. *NPJ Flexible Electronics*, 3(1):7, 2019.

[34] Peiqi Wei, Xiaoliang Guo, Xianbo Qiu, and Duli Yu. Flexible capacitive pressure sensor with sensitivity and linear measuring range enhanced based on porous composite of carbon conductive paste and polydimethylsiloxane. *Nanotechnology*, 30(45):455501, 2019.

[35] Ruilong Shi, Zheng Lou, Shuai Chen, and Guozhen Shen. Flexible and transparent capacitive pressure sensor with patterned microstructured composite rubber dielectric for wearable touch keyboard application. *Sci. China Mater.*, 61(12):1587–1595, 2018.

[36] Jinlong Zhu, Changqing Jin, Wenwu Cao, and Xiaohui Wang. Phase transition and dielectric properties of nanograin batio3 ceramic under high pressure. *Applied Physics Letters*, 92(24), 2008.

[37] Matias Acosta, N Novak, V Rojas, S Patel, R Vaish, J Koruza, GA Rossetti, and JJAP Rödel. Batio3-based piezoelectrics: Fundamentals, current status, and perspectives. *Applied Physics Reviews*, 4(4), 2017.

[38] Han Ding, Chen Qian, Jinsong Han, Ge Wang, Wei Xi, Kun Zhao, and Jizhong Zhao. Rfipad: Enabling cost-efficient and device-free in-air handwriting using passive tags. In *2017 IEEE 37Th international conference on distributed computing systems (ICDCS)*, pages 447–457. IEEE, 2017.

[39] Hanchuan Li, Can Ye, and Alanson P Sample. Idsense: A human object interaction detection system based on passive uhf rfid. In *Proceedings of the 33rd Annual ACM Conference on Human Factors in Computing Systems*, pages 2555–2564, 2015.

[40] Alanson P Sample, Daniel J Yeager, and Joshua R Smith. A capacitive touch interface for passive rfid tags. In *2009 IEEE International Conference on RFID*, pages 103–109. IEEE, 2009.

[41] Yanling Bu, Lei Xie, Yinyin Gong, Chuyu Wang, Lei Yang, Jia Liu, and Sanglu Lu. Rf-dial: Rigid motion tracking and touch gesture detection for interaction via rfid tags. *IEEE Transactions on Mobile Computing*, 21(3):1061–1080, 2020.

[42] Hanchuan Li, Eric Brockmeyer, Elizabeth J Carter, Josh Fromm, Scott E Hudson, Shwetak N Patel, and Alanson Sample. Paperid: A technique for drawing functional battery-free wireless interfaces on paper. In *Proceedings of the 2016 CHI Conference on Human Factors in Computing Systems*, pages 5885–5896, 2016.

[43] Agrim Gupta, Cédric Girerd, Manideep Dunna, Qiming Zhang, Raghav Subbaraman, Tania Morimoto, and Dinesh Bharadia. {WiForce}: Wireless sensing and localization of contact forces on a space continuum. In *18th USENIX Symposium on Networked Systems Design and Implementation (NSDI 21)*, pages 827–844, 2021.

[44] Xiaoran Fan, Daewon Lee, Larry Jackel, Richard Howard, Daniel Lee, and Volkan Isler. Enabling low-cost full surface tactile skin for human robot interaction. *IEEE Robotics and Automation Letters*, 7(2):1800–1807, 2022.

[45] Cecilia Occhiuzzi, Amin Rida, Gaetano Marrocco, and Manos Tentzeris. Rfid passive gas sensor integrating carbon nanotubes. *IEEE Transactions on Microwave Theory and Techniques*, 59(10):2674–2684, 2011.

[46] Sabina Manzari, Alexandro Catini, Giuseppe Pomarico, Corrado Di Natale, and Gaetano Marrocco. Development of an uhf rfid chemical sensor array for battery-less ambient sensing. *IEEE Sensors Journal*, 14(10):3616–3623, 2014.

[47] Cui Zhao, Zhenjiang Li, Han Ding, Ge Wang, Wei Xi, and Jizhong Zhao. Rf-wise: Pushing the limit of rfid-based sensing. In *IEEE INFOCOM 2022-IEEE Conference on Computer Communications*, pages 1779–1788. IEEE, 2022.

[48] Ge Wang, Chen Qian, Jinsong Han, Wei Xi, Han Ding, Zhiping Jiang, and Jizhong Zhao. Verifiable smart packaging with passive rfid. In *Proceedings of the 2016 ACM International Joint Conference on Pervasive and Ubiquitous Computing*, pages 156–166, 2016.

[49] Rahul Bhattacharyya, Christian Floerkemeier, and Sanjay Sarma. Rfid tag antenna based sensing: Does your beverage glass need a refill? In *2010 IEEE International Conference on RFID (IEEE RFID 2010)*, pages 126–133. IEEE, 2010.

[50] Santiago Capdevila, Lluis Jofre, Jordi Romeu, and Jean-Charles Bolomey. Passive rfid based sensing. In *2011 IEEE International Conference on RFID-Technologies and Applications*, pages 507–512. IEEE, 2011.

[51] Ju Wang, Omid Abari, and Srinivasan Keshav. Challenge: Rfid hacking for fun and profit. In *Proceedings of the 24th Annual International Conference on Mobile Computing and Networking*, pages 461–470, 2018.

[52] Yuan He, Yilun Zheng, Meng Jin, Songzhen Yang, Xiaolong Zheng, and Yunhao Liu. Red: Rfid-based eccentricity detection for high-speed rotating machinery. *IEEE Transactions on Mobile Computing*, 20(4):1590–1601, 2019.

[53] Binbin Xie, Jie Xiong, Xiaojiang Chen, and Dingyi Fang. Exploring commodity rfid for contactless sub-millimeter vibration sensing. In *Proceedings of the 18th Conference on Embedded Networked Sensor Systems*, pages 15–27, 2020.

[54] Yilin Liu, Shijia Zhang, Mahanth Gowda, and Srihari Nelakuditi. Leveraging the properties of mmwave signals for 3d finger motion tracking for interactive iot applications. *Proceedings of the ACM on Measurement and Analysis of Computing Systems*, 6(3):1–28, 2022.

[55] Elahe Soltanaghaei, Akarsh Prabhakara, Artur Balanuta, Matthew Anderson, Jan M Rabaey, Swarun Kumar, and Anthony Rowe. Millimetro: mmwave retro-reflective tags for accurate, long range localization. In *Proceedings of the 27th Annual International Conference on Mobile Computing and Networking*, pages 69–82, 2021.

[56] Karthikeyan Sundaresan and Sampath Rangarajan. Locating objects in indoor spaces using radio frequency backscatter tags, April 30 2024. US Patent 11,971,473.

[57] Lei Yang, Qiongzheng Lin, Xiangyang Li, Tianci Liu, and Yunhao Liu. See through walls with cots rfid system! In *Proceedings of the 21st annual international conference on mobile computing and networking*, pages 487–499, 2015.

[58] Wenjie Ruan, Quan Z Sheng, Lina Yao, Xue Li, Nickolas JG Falkner, and Lei Yang. Device-free human localization and tracking with uhf passive rfid tags: A data-driven approach. *Journal of Network and Computer Applications*, 104:78–96, 2018.

[59] Yunfei Ma, Nicholas Selby, and Fadel Adib. Minding the billions: Ultra-wideband localization for deployed rfid tags. In *Proceedings of the 23rd annual international conference on mobile computing and networking*, pages 248–260, 2017.

[60] Haojian Jin, Zhijian Yang, Swarun Kumar, and Jason I Hong. Towards wearable everyday body-frame tracking using passive rfids. *Proceedings of the ACM on Interactive, Mobile, Wearable and Ubiquitous Technologies*, 1(4):1–23, 2018.

[61] Chengkun Jiang, Yuan He, Xiaolong Zheng, and Yunhao Liu. Orientation-aware rfid tracking with centimeter-level accuracy. In *2018 17th ACM/IEEE International Conference on Information Processing in Sensor Networks (IPSN)*, pages 290–301. IEEE, 2018.

[62] Longfei Shangguan, Zhenjiang Li, Zheng Yang, Mo Li, Yunhao Liu, and Jinsong Han. Otrack: Towards order tracking for tags in mobile rfid systems. *IEEE Transactions on Parallel and Distributed Systems*, 25(8):2114–2125, 2013.

[63] Lei Yang, Yekui Chen, Xiang-Yang Li, Chaowei Xiao, Mo Li, and Yunhao Liu. Tagoram: Real-time tracking of mobile rfid tags to high precision using cots devices. In *Proceedings of the 20th annual international conference on Mobile computing and networking*, pages 237–248, 2014.

[64] Teng Wei and Xinyu Zhang. Gyro in the air: tracking 3d orientation of batteryless internet-of-things. In *Proceedings of the 22nd Annual International Conference on Mobile Computing and Networking*, pages 55–68, 2016.

[65] Francesco Piccinno, Federica Naccarata, Riccardo Colella, Francesco P Chietera, Luca Catarinucci, and Gaetano Marrocco. Exploiting self-tunable rfid chips for wireless sensing of permittivity to enable passive low-cost food-quality monitoring systems. In *2023 IEEE 13th International Conference on RFID Technology and Applications (RFID-TA)*, pages 45–48. IEEE, 2023.

[66] Konstantinos Zannas, Hatem El Matbouly, Yvan Duroc, and Smail Tedjini. Self-tuning rfid tag: A new approach for temperature sensing. *IEEE Transactions on Microwave Theory and Techniques*, 66(12):5885–5893, 2018.

[67] Francesco Amato, Carolina Miozzi, Simone Nappi, and Gaetano Marrocco. Self-tuning uhf epidermal antennas. In *2019 IEEE International Conference on RFID Technology and Applications (RFID-TA)*, pages 380–383. IEEE, 2019.

[68] Junbo Zhang, Gaurav Balakrishnan, Sruti Srinidhi, Arnav Bhat, Swarun Kumar, and Christopher Bettinger. Nfcapsule: An ingestible sensor

pill for eosinophilic esophagitis detection based on near-field coupling. In *Proceedings of the 20th ACM Conference on Embedded Networked Sensor Systems*, pages 75–90, 2022.